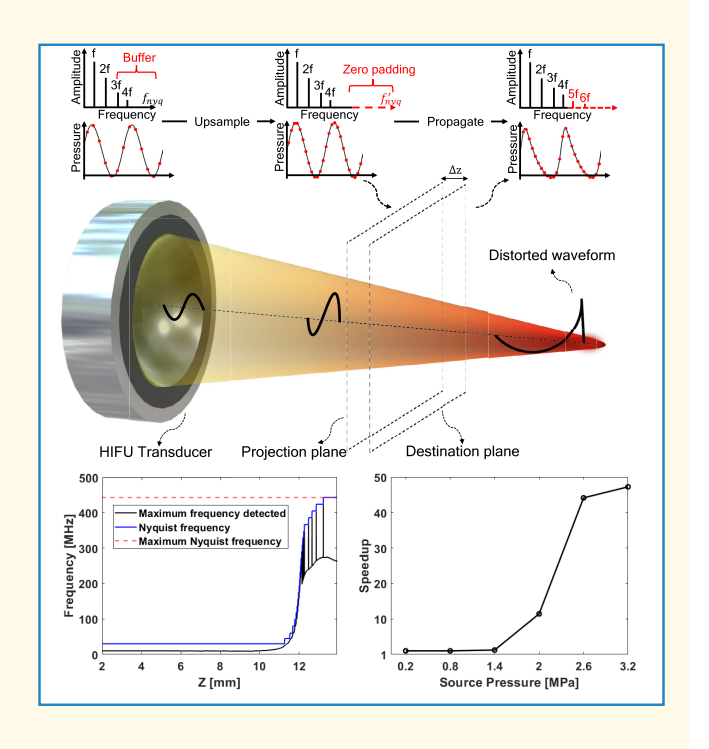


Nonlinear Acoustic Holography With Adaptive Sampling

Ahmed Sallam[®] and Shima Shahab

Abstract—Accurate and efficient numerical simulation of highly nonlinear ultrasound propagation is essential for a wide range of therapeutic and physical ultrasound applications. However, due to large domain sizes and the generation of higher harmonics, such simulations are computationally challenging, particularly in 3-D problems with shock waves. Current numerical methods are based on computationally inefficient uniform meshes that resolve the highest harmonics across the entire spatial domain. To address this challenge, we present an adaptive numerical algorithm for computationally efficient nonlinear acoustic holography. At each propagation step, the algorithm monitors the harmonic content of the acoustic signal and adjusts its discretization parameters accordingly. This enables efficient local resolution of higher harmonics in areas of high nonlinearity while avoiding unnecessary resolution elsewhere. Furthermore, the algorithm actively adapts to the signal's nonlinearity level, eliminating the need for prior reference simulations or information about the spatial distribution of the harmonic content of the acoustic field. The proposed algorithm incorporates an upsampling process in the frequency domain to accommodate the generation of higher harmonics in forward propagation and a downsampling process when higher harmonics are decimated in backward propagation. The efficiency of the algorithm was evaluated for highly nonlinear 3-D problems, demonstrating a significant reduction in computational cost with



a nearly 50-fold speedup over a uniform mesh implementation. Our findings enable a more rapid and efficient approach to modeling nonlinear high-intensity focused ultrasound (HIFU) wave propagation.

Index Terms— Acoustic holograms, acoustic holography, high-intensity focused ultrasound (HIFU), nonlinear ultrasound.

I. INTRODUCTION

COUSTIC holography is a technique that enables the reconstruction of 3-D acoustic fields by projecting measured or simulated 2-D data from the hologram plane to the rest of the volume. Accurate and efficient nonlinear acoustic holography of high-intensity ultrasound is an essential tool for a wide range of applications in the fields of

Manuscript received 28 July 2023; accepted 9 September 2023. Date of publication 13 September 2023; date of current version 9 November 2023. This work was supported by the U.S. National Science Foundation (NSF) through CAREER grant under Award CMMI 2143788. (Corresponding author: Shima Shahab.)

The authors are with the Department of Mechanical Engineering, Virginia Tech, Blacksburg, VA 24060 USA (e-mail: ahmedsallam@vt.edu; sshahab@vt.edu).

Digital Object Identifier 10.1109/TUFFC.2023.3315011

medical and physical acoustics [1], [2], [3], [4], [5], [6]. In high-intensity focused ultrasound (HIFU) therapy, it is critical to characterize and model the nonlinear pressure field to establish therapeutic protocols and to predict the ultrasound-induced biological effects [7], [8], [9].

Acoustic holography is also widely used in source synthesis and identification due to its exceptional ability to visualize and analyze complex 3-D sound fields. Holographic techniques are used to compute the necessary phase and/or amplitude maps to create desired sound-field structures. These structures are then physically realized using either phased array transducers or passive acoustic devices such as holographic lenses or metasurfaces, which enable arbitrary sound beam shaping and patterning [10], [11], [12], [13], [14], [15], [16], [17]. Such techniques have been used in various applications, including

Highlights

- Simulating high-intensity ultrasound is computationally expensive. We introduce an adaptive algorithm that significantly reduces the computation time by using more efficient sampling techniques.
- The algorithm monitors the harmonic content of the signal and adjusts the discretization parameters. A speed-up
 of up to 50-fold was achieved compared to uniform mesh implementation.
- The algorithm has numerous applications in nonlinear medical and physical acoustics. It allows for rapid and accurate source characterization and prediction of sonication dosage and thermal effects.

particle levitation and lithotripsy [18], [19], in which nonlinear effects such as acoustic streaming and harmonic generation are present. Nonlinear acoustic holography is also used for source identification, allowing for the examination of the locations and characteristics of radiating surfaces for high-level noise diagnostics and shock-wave control [20]. In addition, nonlinear acoustic holography is used for computing the propagation of higher harmonics, which is essential in nonlinear imaging applications, such as harmonic imaging and diagnostics [21].

However, simulating the propagation of nonlinear acoustic fields is a computationally challenging problem [1], [7], [22]. Often the computational domain is much larger than the smallest wavelength present. Moreover, the nonlinear problem requires the use of extremely fine spatial and temporal discretization to accurately capture the generated harmonics. As a result, the computational cost quickly escalates, especially for 3-D problems. A large number of harmonics should be considered when steep shock-wave fronts are present. Resolving up to several hundred harmonics is required if the propagating medium is highly nonlinear with low frequency-dependent attenuation, such as water. However, in media such as soft tissue, where higher harmonics are more strongly attenuated, the requirements for the number of harmonics are less stringent [22]. Significant efforts have been made to reduce the computational cost of such simulations.

Tavakkoli et al. [23], [24] introduced computationally efficient models based on a second-order operator splitting approach, with a fractional step-marching scheme, capable of simulating finite-amplitude ultrasound beam propagation in water and tissue. Wherein linear and nonlinear effects are propagated separately over incremental steps, and the computation of the diffractive substeps is based on an angular spectrum technique for accurate and efficient implementation of diffractive propagation from nonaxially symmetric sources. However, modeling of the shock fronts often requires a very dense temporal sampling [25]. Adaptive meshes and nonuniform step sizes may further reduce computational cost [26], especially when considering full 4-D (three dimensions of space and time) field simulations.

Since nonlinear effects are highly localized around the focal point [27], very fine discretization is only required locally in the computational domain at the regions that exhibit the highest nonlinearity and harmonic content. Recent techniques used computationally efficient nonuniform spatial

meshes with more refined numerical discretization in regions with the highest nonlinearity [7], [28], [29]. Overall, this can result in a significant reduction in the total number of grid points, and thus memory and execution time without compromising accuracy. However, current techniques for designing nonuniform meshes require prior knowledge of the spatial distribution of the harmonics in the ultrasound field. Because the ultimate goal of such techniques is to eliminate the need to carry out reference simulations on computationally inefficient uniform meshes, a reference simulation on a priori basis is assumed to be unavailable. In addition, such simulations would require mesh convergence investigations since the actual harmonic content of the signal cannot be predicted accurately, adding to the computational burden. Furthermore, when patterns with complex focal zones are considered, or when backward propagation is used to identify sources of unknown locations or characteristics, the problem of designing a nonuniform mesh becomes increasingly difficult.

The adaptive nonlinear acoustic holography (ANAH) algorithm is introduced in this article as a novel approach to nonlinear acoustic holography simulations. At each propagation step, the ANAH algorithm actively monitors the harmonic content of the wavefront and adjusts the discretization parameters as needed. Other than basic parameters such as propagation medium and fundamental excitation frequency, such implementation eliminates the need for reference simulations or prior knowledge of the ultrasound field. We will demonstrate ANAH for capturing shock-wave fronts in three dimensions, which is a significant challenge in nonlinear acoustics. In addition, we will show how ANAH can be used for backward propagation in source identification applications.

This article is structured as follows: Section II-A outlines the mathematical model used for the nonlinear forward and backward propagations, and Section II-B introduces the proposed adaptive algorithm. In Section III, we validated and investigated the performance of the ANAH algorithm for forward and backward propagations. We also discuss the most important parameters in the algorithm and their effects on the computation speed and accuracy. Finally, in Section IV, we summarize, conclude the present work, and discuss future directions.

II. THEORY

A. Forward and Backward Projection

The wave-vector frequency-domain method [30], [31], [32] is implemented to carry out the nonlinear forward and

backward propagations. This approach is based on the generalized Westervelt equation and can be considered an extended version of the angular spectrum method. The acoustic field is computed by marching in the spatial domain along the axis normal to the source plane.

Starting with the generalized Westervelt equation

$$\rho \nabla \cdot \left(\frac{1}{\rho} \nabla p\right) - \frac{1}{c^2} \frac{\partial^2 p}{\partial t^2} + \frac{\delta}{c^4} \frac{\partial^3 p}{\partial t^3} + \frac{\beta}{\rho c^4} \frac{\partial^2 p^2}{\partial t^2} = \gamma \frac{\partial p}{\partial t}$$
 (1)

where p is the acoustic pressure, ρ is the ambient density, c is the speed of sound, δ is the sound diffusivity, and β is the nonlinearity coefficient. The frequency-independent absorption term $\gamma \partial p/\partial t$ accounts for the absorption layer close to the computational boundary [33]. Applying the normalized wavefield $f = p/\sqrt{\rho}$ and performing the Fourier transform with respect to X, Y, and t yields

$$\frac{\partial^{2}}{\partial Z^{2}}\tilde{F} + K^{2}\tilde{F}$$

$$= F_{XY} \left\{ \left[\sqrt{\rho} \nabla^{2} \frac{1}{\sqrt{\rho}} - \frac{\omega^{2}}{c_{0}^{2}} \left(\frac{c_{0}^{2}}{c^{2}} - 1 \right) + \frac{i\delta\omega^{3}}{c^{4}} + i\omega\gamma \right] F_{t}(f) \right\}$$

$$+ F_{XY} \left(\frac{\beta\omega^{2}}{\rho c^{4}} F_{t}(f^{2}) \right) \tag{2}$$

where \tilde{F} is the Fourier transform of f, F_{XY} is the Fourier transform operator in the X- and Y-dimensions, F_t is the Fourier transform operator in the time domain, c_0 is the background sound speed, and $K^2 = \omega^2/c_0^2 - k_X^2 - k_Y^2$, where k_X and k_Y are the wavenumbers in the X- and Y-dimensions, respectively. An implicit, one-way propagation can be derived from 1-D Green's function in the form of an integral equation [32], such that

$$\tilde{F}(Z) = \tilde{F}(0)e^{iKZ} + \frac{e^{iKZ}}{2iK} \int_0^Z e^{-iKZ'} M(f(Z')) dZ'$$
 (3)

where

$$M(f) = F_{XY} \left\{ \left[\sqrt{\rho} \nabla^2 \frac{1}{\sqrt{\rho}} - \frac{\omega^2}{c_0^2} \left(\frac{c_0^2}{c^2} - 1 \right) + \frac{i\delta\omega^3}{c^4} + i\omega\gamma \right] F_t(f) \right\} + F_{XY} \left(\frac{\beta\omega^2}{\sqrt{\rho}c^4} F_t(f^2) \right). \tag{4}$$

Equation (3) is solved using a Simpson-like rule [30], [34]. The pressure distribution on the source plane or any arbitrary plane is reconstructed using the backward projection. By changing Z in (3) to -Z, the backward projection is obtained as

$$\tilde{F}(-Z) = \tilde{F}(0)e^{-iKZ} - \frac{e^{-iKZ}}{2iK} \int_0^{-Z} e^{iKZ'} M(f(-Z')) dZ'.$$
(5)

Using this model, wave effects such as full-wave diffraction, attenuation, dispersion, and nonlinearity are considered, including nonlinearity in arbitrary directions, making it particularly accurate for highly focused transducers [32]. The present formulation only includes one-way propagation with no reflections making it only accurate for modeling wave propagation in weakly heterogeneous media [34]. Phase

correction, amplitude compensation, and multiple reflections were later incorporated with the one-way model to improve the accuracy for strongly heterogeneous media such as transcranial ultrasound propagation [35].

The Kramers–Kronig dispersion relationship is applied directly by replacing the speed of sound c with c_p and $c_p = (1/\hat{c} + \alpha_0 \tan(\pi y/2)\omega^{y-1})^{-1}$, where \hat{c} is the sound speed at zero frequency, y is the power-law exponent, α_0 is the absorption in nepers per megahertz^{-y} per meter, and $\alpha_o = \alpha_{NP}\omega^{-y}$.

B. Adaptive Algorithm

The acoustic field calculations are performed in both the temporal and frequency domains by numerically propagating the field onto parallel projection planes along the propagation axis. The axial distance between each projection plane, i.e., the step size ΔZ , should be small enough to ensure the stability and accuracy of the numerical scheme [31]. In the temporal domain, the time resolution Δt should adhere to the Nyquist-Shannon sampling theorem, which states that under perfect conditions, a harmonic signal can be perfectly reconstructed when sampled at a rate of two points per period of its highest frequency $\Delta t = 1/2 f_{\text{max}}$. In this case, f_{max} is the frequency of the highest generated harmonic. In the case of highly nonlinear fields with shock waves, a large number of harmonics must be considered (up to hundreds of harmonics for shock-wave modeling) as such an extremely small step size ΔZ and temporal resolution Δt is necessary, which could lead to unfeasible long computation time, especially in 3-D problems. In addition, the Gibbs effect occurs when insufficient harmonics represent shock waves. The errors are typically manifested as highfrequency oscillations near the shock discontinuity. This causes instability in the numerical scheme along with amplification and accumulation of errors along the planar projection [36].

To this end, we present an adaptive algorithm that adjusts the discretization parameters ΔZ and Δt according to the highest harmonic detected in the acoustic signal. The adaptive algorithm implements a monitoring function that tracks the frequency of the highest harmonic $f_{\rm max}$ in the signal at each propagation step. This maximum is extracted by finding the frequency of the highest harmonic with an amplitude larger than a threshold value. The threshold value $A_{\rm Th}$ is directly related to the amplitude of the fundamental and can be expressed as $A_{\rm Th} = A_F R_h$, where A_F is the amplitude of the fundamental, and R_h is a chosen fraction value. A smaller R_h means a lower threshold value which leads to more harmonics being included.

To avoid aliasing errors and minimize the Gibbs effect, the algorithm maintains a spectral buffer b between the frequency of the highest harmonic $f_{\rm max}$ and the Nyquist frequency $f_{\rm Nyq}$, such that $f_{\rm Nyq} > f_{\rm max} + b$. As the wave propagates and more harmonics are generated, $f_{\rm max}$ increases and oversteps into the buffer region such that $f_{\rm Nyq} > f_{\rm max} \geq f_{\rm Nyq} - b$. To accommodate the newly generated harmonics and maintain the accuracy of the simulation, the original time signal is

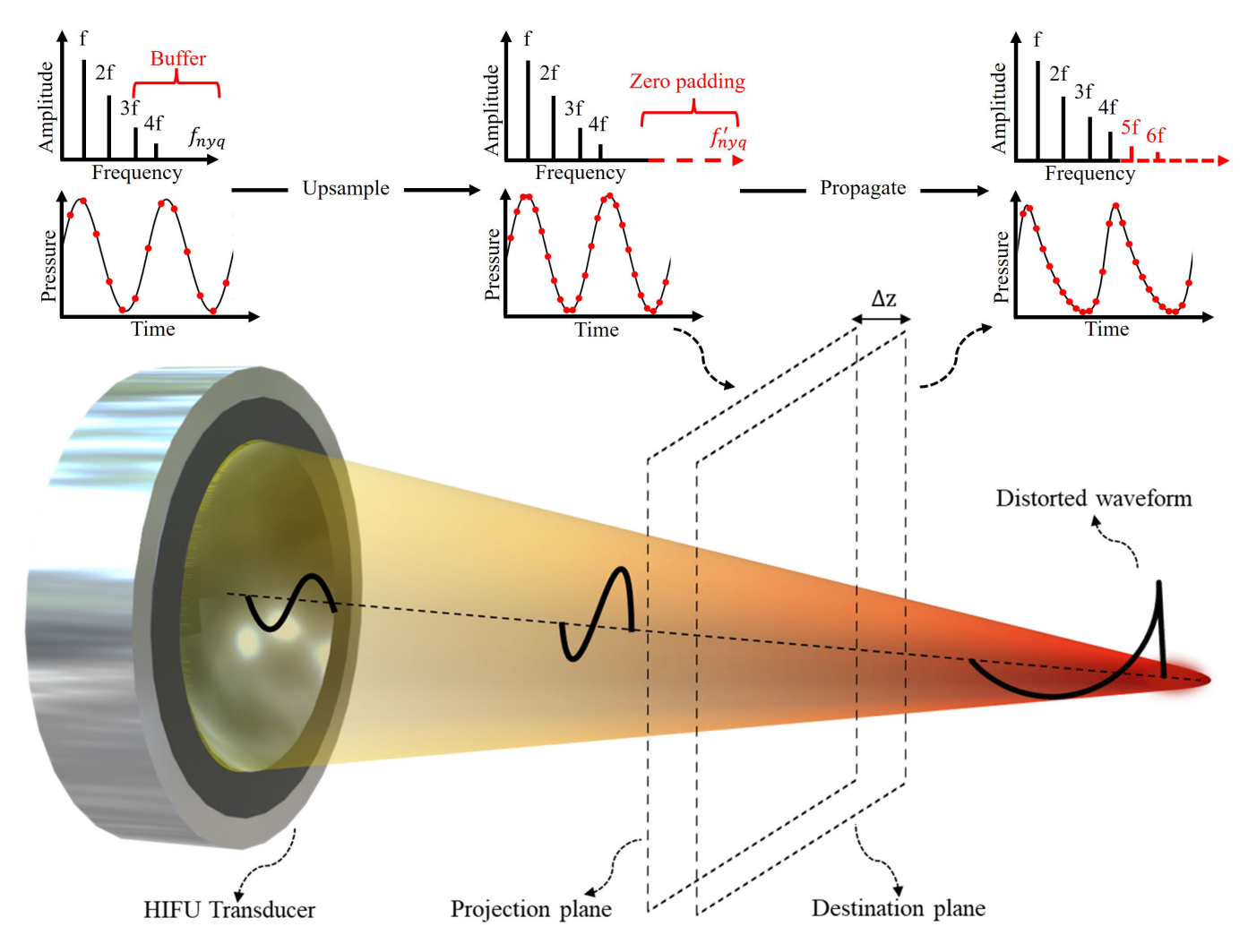


Fig. 1. Schematic representation of focused ultrasound nonlinear acoustic wave propagation of an initially linear wave (bottom left) to a highly distorted waveform at the focal point (bottom right). The upsampling of the signal in the frequency domain is also illustrated (top). As the higher harmonics overstep into the spectral buffer zone (top left), the signal is interpolated by zero-padding the spectrum (top middle). The wave is then nonlinearly propagated forward from the projection plane to the destination plane, and the newly generated higher harmonics can be resolved due to the upsampling process.

interpolated to increase the original sampling rate and Nyquist frequency such that $\Delta t' = 1/(2(f_{\text{max}} + n_h f_0))$ and $f'_{\text{Nyq}} = f_{\text{max}} + n_h f_0$. Where $\Delta t'$ and f'_{Nyq} are, respectively, the sampling rate and Nyquist frequency of the interpolated signal, and f_0 is the fundamental frequency. The size of the spectral padding $n_h f_0$ is a function of the fundamental frequency f_0 and the positive integer n_h , such that at each adaptive step, the Nyquist frequency is increased by n_h harmonics. For computational efficiency, the interpolation is carried out in the frequency domain by zero-padding the original spectrum of the signal [37], [38]. Let us consider an initial wave signal $p[n], n = 0, 2, \ldots, L - 1$ where n is the time index, and L is the sample length. The discrete Fourier transform (DFT) of p[n] is defined as

$$P[k] = \sum_{n=0}^{L-1} p[n]e^{-2\pi jkn/L}$$
 (6)

where P[k] is the complex frequency-domain representation of the signal, k is the frequency index, and j is the

imaginary unit. In addition, the inverse DFT (IDFT) is defined as

$$p[n] = \frac{1}{L} \sum_{n=0}^{L-1} P[k] e^{2\pi j k n/L}.$$
 (7)

Note that the scaling by 1/L is included in the IDFT, which is the same choice as in MATLAB's FFT and IFFT implementations.

When the spectrum of a signal is appended with zeros, the IDFT effectively applies the aliased sinc function for time-domain interpolation [37]. The original spectrum is zero-padded, as illustrated in Fig. 1. The modified spectrum P'[k] has length $N' = N(\Delta t/\Delta t')$ where N is the number of samples in the original spectrum. The modified spectrum P' retains all the information of the original spectrum P and is padded with exactly N' - N - 1 zeros filling the high-frequency part of the spectrum.

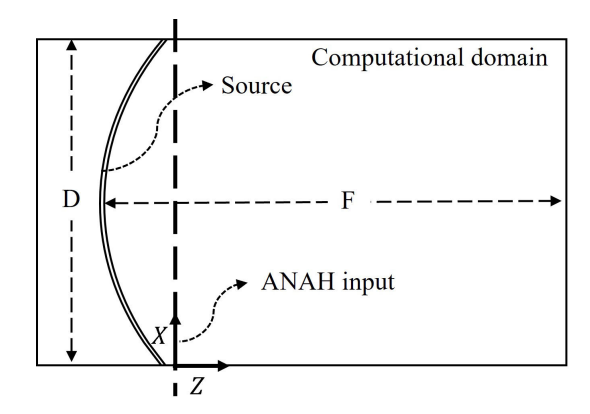


Fig. 2. Schematic illustration of the computational domain, the simulated focused ultrasound transducer, and the input plane used to initialize the ANAH algorithm.

The construction of the modified spectrum is described in the following equations [37], [38]:

$$P'(k) = \begin{cases} \left(\Delta t'/\Delta t\right) P(k), & 0 \le k < \frac{N}{2} \\ \frac{1}{2} \left(\Delta t'/\Delta t\right) P\left(\frac{N}{2}\right), & k = \frac{N}{2} \\ 0, & \frac{N}{2} < k < N' - \frac{N}{2} \\ \frac{1}{2} \left(\Delta t'/\Delta t\right) P\left(\frac{N}{2}\right), & k = N' - \frac{N}{2} \\ \left(\Delta t'/\Delta t\right) P(k - N' + N), & N' - \frac{N}{2} < k < N'. \end{cases}$$
(8)

Such construction retains Hermitian symmetry; thus, the result of the IDFT is a real-valued signal.

In backward propagation, the initially nonlinear signal is propagated back to the source plane, causing higher harmonics to be decimated. As a result, the signal is downsampled by the adaptive algorithm to account for the reduction in harmonic content. This downsampling approach improves computational efficiency while maintaining accuracy in nonlinear acoustic holography simulations. The downsampling is also accomplished in the frequency domain by truncating part of the spectrum. Only the spectral information up to the new Nyquist frequency is retained. The monitoring function triggers the downsampling process when the relationship $G < f_{\text{Nyq}} - f_{\text{max}}$ is true. G represents the maximum allowed spectral gap between the Nyquist frequency f_{Nyq} and the frequency of the highest harmonic f_{max} before the signal is truncated. The new sample rate and Nyquist frequency of the truncated signal are expressed as $\Delta t' = 1/(2(f_{\text{Nyq}} - G))$ and $f'_{\text{Nyq}} = f_{\text{Nyq}} - G$. The spectral truncation process is described in the following equation [37], [38]:

$$P'(k) = \begin{cases} \left(\Delta t'/\Delta t\right) P(k), & \text{for } 0 \le k < \frac{N'}{2} \\ 0, & \text{for } k = \frac{N'}{2} \\ \left(\Delta t'/\Delta t\right) P(N-N'+k), & \text{for } \frac{N'}{2} < k \le N'-1. \end{cases}$$

Finally, in both the back and front propagations, the value of the step size ΔZ is also updated according to the new Nyquist frequency such that $\Delta Z' = c/2f'_{\rm Nyq}$. The spatial resolutions ΔX and ΔY are fixed throughout the propagation process since the discretization requirements are not as strict when the propagation direction is mainly along the axis of the transducer. [31], [32].

III. RESULTS AND DISCUSSION

A. Validation

To verify our approach, we simulated a single-element spherically focused ultrasound transducer. The simulation results of the ANAH algorithm were examined by comparing the obtained data with full-wave numerical simulations based on the k-space pseudospectral method [39]. The numerical model solves a set of coupled partial differential equations equivalent to a generalized Westervelt equation. The accuracy and validity of this numerical model have been previously verified with analytical solutions and experimental measurements [40], [41]. The pseudospectral method was implemented using the open-source MATLAB Toolbox kwave, which is available online [42] (the performance of the C++ version when running axisymmetric simulations with nonsquare domains is orders of magnitude slower due to peculiarities with the discrete trigonometric transforms in Intel MKL [43]). The pseudospectral method was used to perform homogeneous axisymmetric nonlinear acoustic simulations with power-law absorption [44]. The numerical computations were carried out at an excitation frequency of 1 MHz, and the propagation medium was modeled using the following physical parameters: $\rho_0 = 1000 \text{ kg/m}^3$, $c_0 =$ 1500 m/s, $\beta = 3.6$, $\alpha_0 = 0.05$ dB/MHz, and $\gamma = 2$. Here ρ_0 , c_0 , and β are the density, ambient speed of sound, and nonlinearity coefficient, respectively. While α_0 and γ , respectively, are the absorption coefficient and the powerlaw exponent. The medium parameters are close to those of water. Highly attenuating media, such as soft tissue, are considered later in this article. The spatial dimensions of the computational domain are 20 × 20 mm, corresponding to the radial and axial directions with a spatial discretization of 500 grid points per wavelength ($dx = 3 \mu m$) and a Courant– Friedrichs-Lewy (CFL) number of 0.25. In addition, perfectly matched layers (PMLs) were added to prevent any reflections at the boundaries. The modeled focused transducer has a focal length and outer diameter of 18 mm ($F_{\#}=1$). The pressure data at a plane with an axial offset of z = 4 mm away from the source are obtained from k-wave simulations and were used as the input to the ANAH algorithm, as shown in Fig. 2.

For computational efficiency, k-wave simulations were computed in axisymmetric coordinates. However, all the ANAH simulations were carried out in the full spatial domain with the 3-D coordinates (i.e., X, Y, and Z) with $n_h = 20$ and $R_h = 0.002$. Here, we note that the axisymmetric cases are considered to enable efficient validation study, and ANAH is not limited to axisymmetric acoustic fields or geometries. Hence, ANAH allows the computation of more complex nonlinear ultrasound propagation and the inclusion

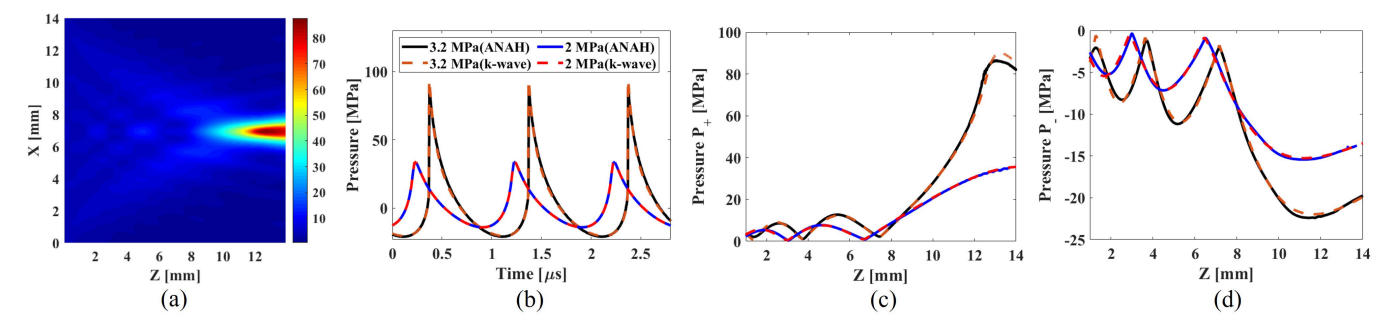


Fig. 3. Comparison of the ANAH algorithm with k-wave results. (a) Axial cross section of the obtained peak positive pressure using ANAH for a source pressure of $P_0 = 3.2$ MPa. Comparison of (b) pressure time waveforms, (c) axial peak positive pressure, and (d) axial peak negative pressure for source pressures of $P_0 = 2$ and 3.2 MPa.

of elaborate geometries in the computational domain. Two simulations were carried out for the cases of a moderately nonlinear field at a source pressure of $P_0 = 2$ MPa and a highly nonlinear field with shock fronts at a source pressure of $P_0 = 3.2$. Planar sources with these amplitudes correspond to Gol'dberg numbers [45] (\bar{z}/ℓ_{α}) , where \bar{z} is the shock formation distance and ℓ_{α} is the absorption length) of 380 and 606, respectively. Fig. 3(a) shows the axial cross section of the simulated field using the ANAH algorithm for $P_0 = 3.2$ MPa. The steady-state time waveforms at the point of maximum peak positive pressure are compared in Fig. 3(b). Good agreement is observed between the k-wave simulations and ANAH for the case of moderate and high nonlinearity. Furthermore, the peak positive and peak negative axial pressures are compared in Fig. 3(c) and (d), respectively. To compare the axial pressures quantitatively, the L_2 -norm errors of the peak positive and peak negative axial pressures were calculated. Here, the relative error norm L_2 is defined as $L_2 = \|p_{\text{ref}}(z_i) - p(z_i)\|_2 / \|p_{\text{ref}}(z_i)\|_2$. For $P_0 = 2$ MPa, the error norms calculated were $L_2 = 1.6\%$ and 2.3% for the axial peak positive and peak negative pressures, respectively. When the source pressure is increased to $P_0 = 3.2$ MPa, the error norms calculated were $L_2 = 3.8\%$ and 2.59% for the axial peak positive and peak negative pressures, respectively. It is noted that for the highly nonlinear case, the k-wave results show approximately 4% higher peak positive pressure around the focal region, as shown in Fig. 3(b) and (c). We attribute this error to the observed Gibbs oscillations and overshoot at the shock front in the k-wave simulations. Including more harmonics in the k-wave simulations would minimize such effects. However, it is computationally prohibitive to include more harmonics. In the current study, 250 harmonics were considered in the k-wave simulations with a total simulation time of 92 h. Nevertheless, the simulation results of the ANAH and k-wave are in overall good agreement for the moderately and highly nonlinear cases.

B. ANAH Performance

To showcase the effectiveness of the proposed ANAH in enhancing the computational efficiency of nonlinear simulations, a comparison is made between its performance and that of equivalent simulations carried out on uniform meshes. To examine the effect of nonlinearity level on the

performance of the algorithm, the simulations were carried out for source pressures that range from $P_0 = 0.2$ to 3.2 MPa. Fig. 4(a) illustrates the maximum harmonic detected within the computational domain via the monitoring function as the source pressure increases. As expected, the rise in acoustic intensity results in an increase in nonlinearity level and the generation of more harmonics. Fig. 4(b) shows the evolution of the detected harmonic content in the acoustic field as the wave propagates to the focal point. The ANAH algorithm progressively adjusts the Nyquist frequency to resolve higher harmonics only when they are detected by the monitoring function. This is in contrast to a uniform mesh where the highest harmonic (illustrated dotted red line) must be resolved throughout the entire computational domain. In Fig. 4(b), it can also be observed that when approaching shock, a large number of harmonics are generated with much smaller amplitudes compared with the fundamental. This could lead to erroneous detection of the highest harmonics in a single spatial step. As we will show later, this behavior is not observed when highly attenuating media are considered. Furthermore, since the harmonic content decreases post-shock, implementing a two-way resampling scheme to reduce sampling beyond the focal region is possible and could improve computational performance. This is, however, more challenging to apply for more complex fields with multifocal regions. In addition, the stability of the adaptive algorithm is essential for applying such a scheme appropriately. The effectiveness of the ANAH algorithm, in comparison to a uniform mesh implementation, is directly related to the degree of localization of the nonlinear effects. To evaluate the degree of localization, we implement the frequency reduction measure (FRM), which is defined as:

$$FRM = \frac{1}{z} \int_{0}^{z} 1 - f_{nyq}(z') / f_{max} dz'$$
 (10)

where $f_{\rm nyq}(z')$ is the Nyquist frequency at each propagation step. FRM varies between 0 for the linear case where the local Nyquist frequency equals the maximum overall frequency in the whole domain (i.e., the adaptive algorithm was not active) and 1 in the case where the local Nyquist frequency was infinitely smaller than the maximum frequency; in this case, the adaptive algorithm will have the highest performance improvement.

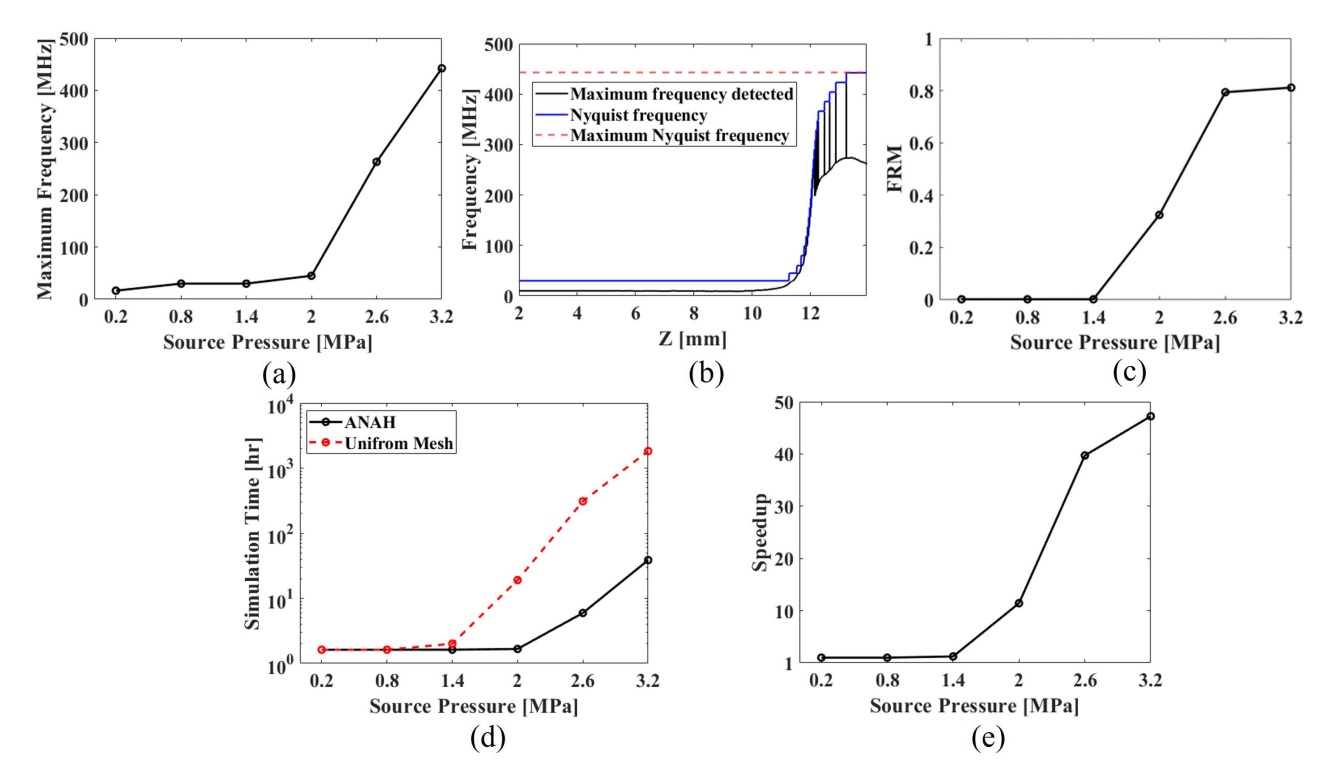


Fig. 4. Evaluation of the ANAH performance compared with a uniform mesh implementation. (a) Frequency of the highest detected harmonic as the source pressure increases. (b) Harmonic content and the adjusted Nyquist frequency as the acoustic field is propagated toward the focal point for $P_0 = 3.2$ MPa. (c) FRM as the source pressure increases. (d) Comparison between the simulation times of the ANAH and uniform mesh implementations as the source pressure increases. (c) Speedup of the simulation time when ANAH is implemented as the source pressure increases

Fig. 4(c) shows the calculated FRM as the source pressure increases. Initially, when the acoustic field is linear, the FRM equals zero since the local nonlinear effects are not present. However, as the source pressure is increased, nonlinearities and their localization increase, and an FRM of 0.82 is calculated at $P_0 = 3.2$ MPa.

As expected, the simulation times shown in Fig. 4(d) illustrate how using uniform meshes scales unfavorably as nonlinearities grow compared with ANAH implementation. Furthermore, Fig. 4(e) shows the speedup in the simulation time when using the ANAH versus the uniform mesh. This speedup follows a similar trend to the FRM, revealing the ANAH's effectiveness, particularly at high nonlinearities, where the ANAH simulation executes nearly 50 times faster than the equivalent uniform mesh implementation at a source pressure of $P_0 = 3.2$ MPa. Furthermore, the results also show that the monitoring function has minimal computational overhead, as both the implementations exhibit almost identical execution times when the field is linear for $P_0 = 0.2$ MPa. We should point out that the uniform mesh simulations were only run for the first ten propagation steps. By taking into account the total number of propagation steps in the entire simulation, the total simulation time using a uniform mesh can be predicted. The computation time required to run the full simulations with a uniform mesh is prohibitively long (up to 1500 h).

To gain a better understanding of the adaptive behavior of the algorithm, we investigate the influence of its primary parameters, namely, n_h and R_h , on the simulation time and accuracy. This investigation focuses on the highest nonlinearity level, with $P_0 = 3.2$ MPa. As depicted in Fig. 5(a) and (b), the maximum Nyquist frequency and the simulation time are mainly influenced by the selection of R_h . However, when the convergence of the maximum peak positive in the simulation is considered, Fig. 5(c) clearly shows that the value of n_h has a significant impact on the simulation accuracy.

When $n_h = 20$ is considered, the maximum convergence error is calculated to be 2.3% for the largest value of $R_h =$ 0.005. However, for $n_h = 5$, the convergence error increases significantly and ranges from 18.5% to 5% for $R_h = 0.005$ and 0.002, respectively. As such, convergence was not achieved for $n_h = 5$ even when R_h is minimized. For $n_h = 10$ and 15, the large convergence error is diminished when R_h is minimized to a value of $R_h = 0.002$. When n_h is set to a value that is too low, the adaptive algorithm fails to match the actual generation rate of the harmonics in the domain, leading to significant inaccuracies in the simulation and a large convergence error. Furthermore, it should be noted that increasing the value of n_h may be a more advantageous approach in achieving accurate simulation results, as opposed to solely minimizing R_h . This is due to the fact that as we showed, an increase in n_h does not significantly affect the computational time, yet has a significant impact on the accuracy of the simulation results. This investigation highlights that using a larger spectral buffer (represented by a larger value of n_h) offers the potential to achieve accurate simulations

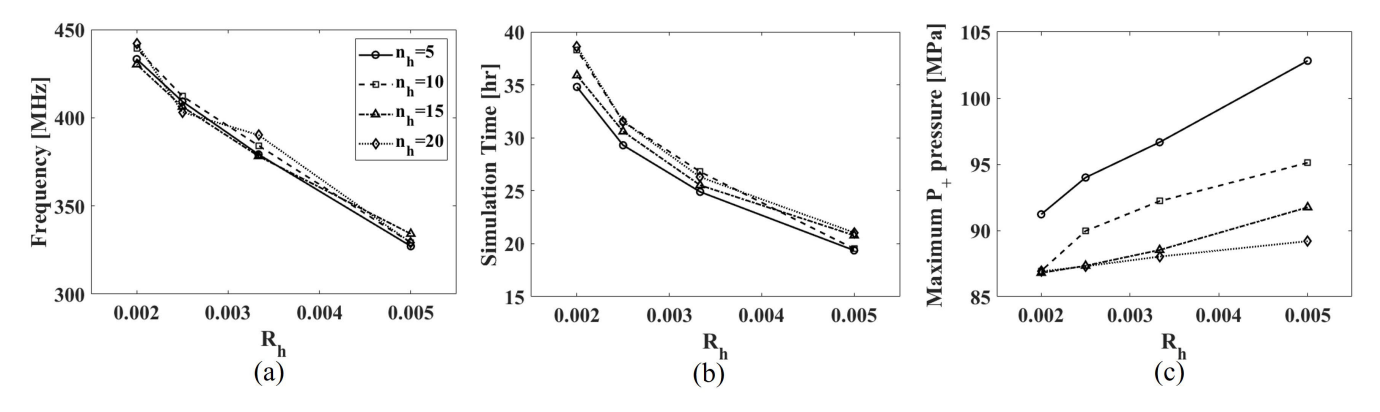


Fig. 5. Effects of the adaptive parameters on the simulation time and accuracy of ANAH at $P_0 = 3.2$ MPa. (a) Maximum Nyquist frequency, (b) total execution time, and (c) convergence of the maximum peak positive as a function of the adaptive parameters.

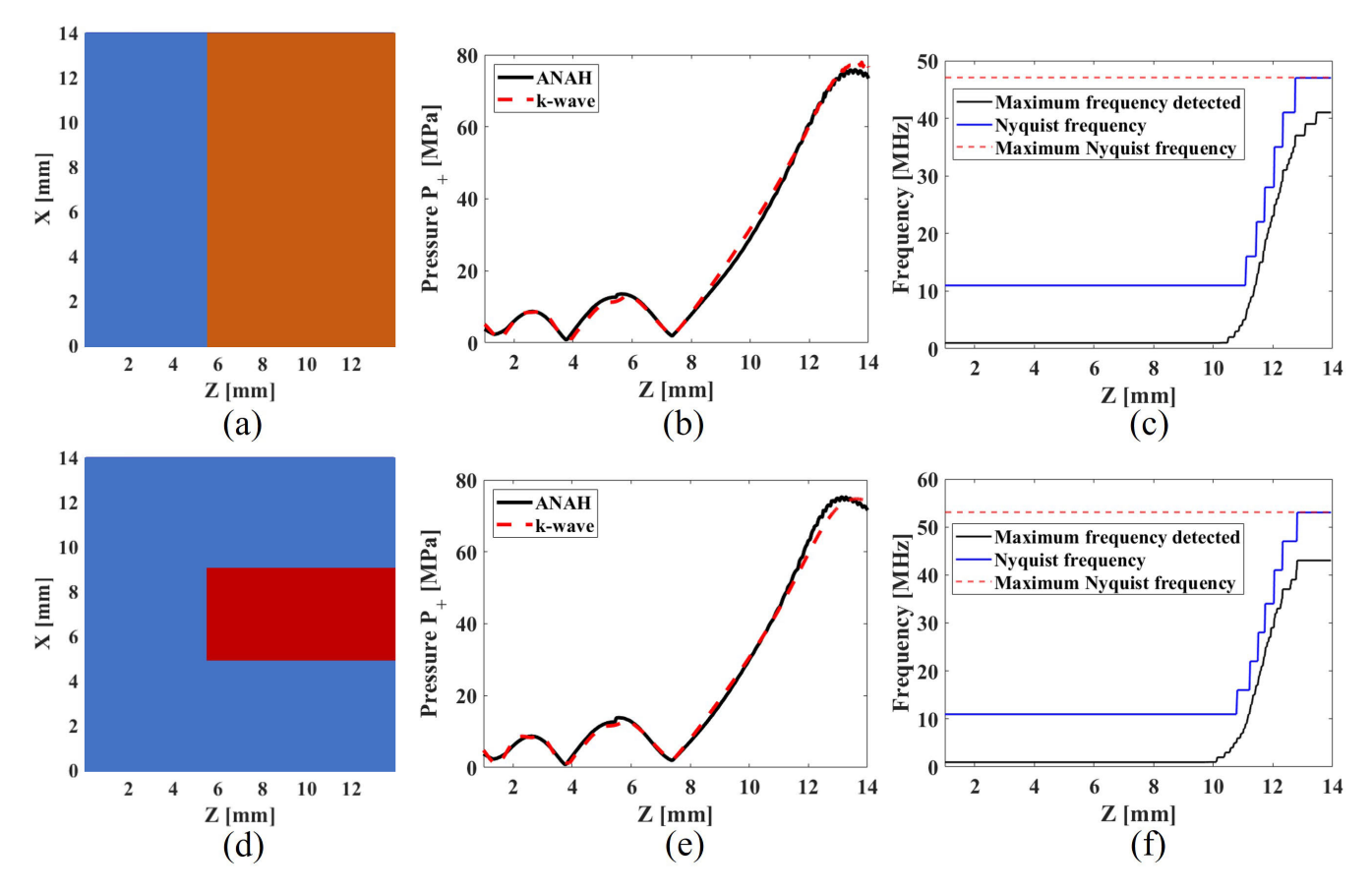


Fig. 6. Evaluation of ANAH for weakly heterogeneous propagation media. (a) Geometry of the multi-layercase, the blue part is the water-like medium, and the orange part represents the liver tissue. (b) Axial peak positive pressure and (c) harmonic content of the simulated multilayer medium. (d) Geometry of the cylindrical tumor, the blue part is the water-like medium, and the red part represents the tumor. (e) Axial peak positive pressure and (f) harmonic content of the simulated water-tumor medium.

without the need for overly sensitive detection (indicated by a smaller value of R_h). This approach allows for better accuracy while maintaining manageable simulation time. Therefore, choosing the appropriate values for n_h and R_h is crucial for achieving accurate and efficient simulations.

C. Weakly Heterogeneous Media

To validate and demonstrate the performance of the proposed ANAH algorithm for more realistic heterogeneous

media and highly attenuating soft tissue, two cases are considered. In the first case, we consider a multilayer geometry with a water-like medium in the first layer and liver tissue in the second layer, as shown in Fig. 6(a). In the second case, a water-like background medium is considered with a cylindrically shaped tumor tissue, as shown in Fig. 6(d). The corresponding acoustic properties of each medium are summarized in Table I [46]. A power-law exponent of 2 is assumed for all the media due to the limitations of the k-wave axisymmetric formulation [44]. For source pressure of

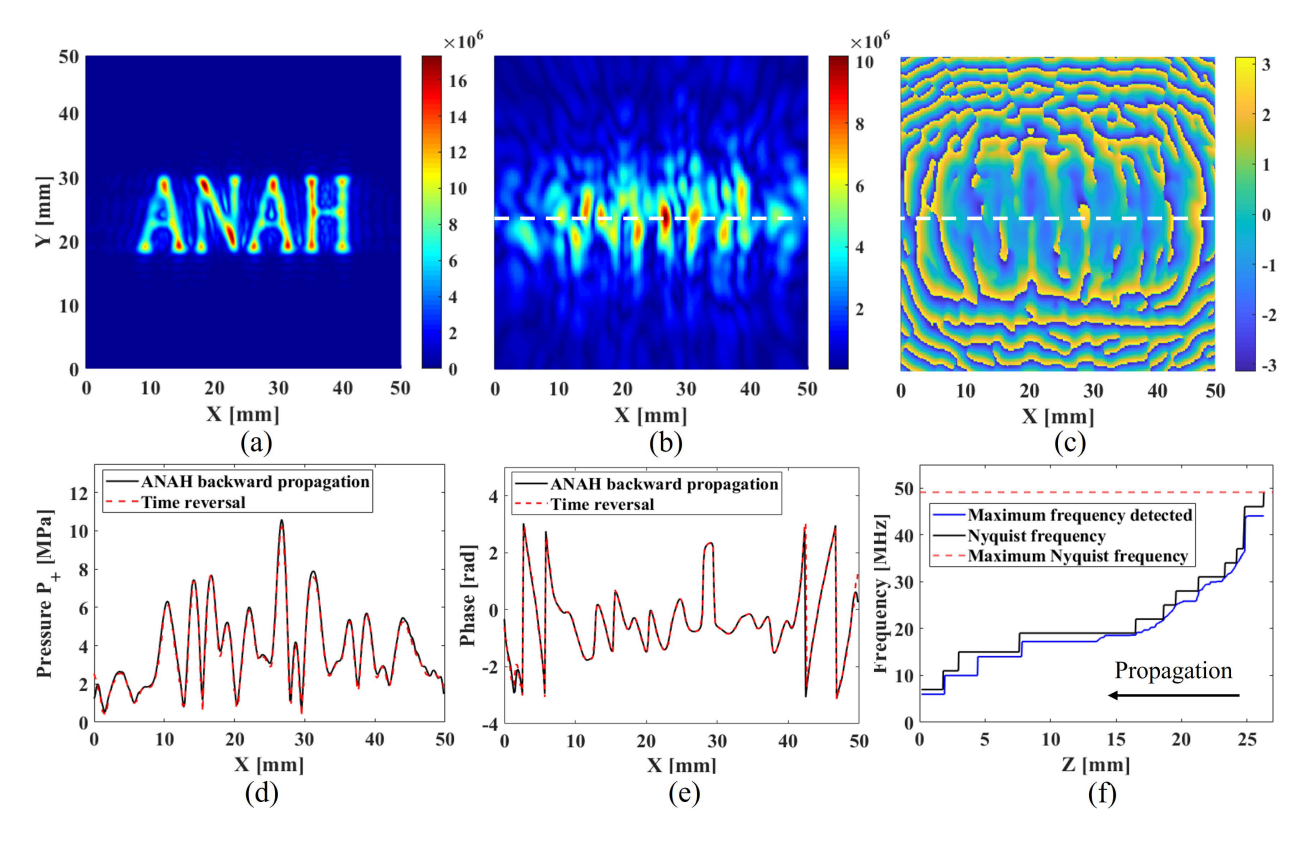


Fig. 7. Illustrating ANAH for backward propagation of nonlinear acoustic fields. (a) "ANAH"-shaped amplitude structure at the image plane constructed by time reversal. (b) and (c) Peak positive pressure and phase at the source plane obtained using time reversal. (d) and (e) Comparison of the peak positive pressures and phases along the dashed line of the initial source pressure and the backward projected field using ANAH. (f) Harmonic content and the adjusted Nyquist frequency as the acoustic field is back propagated to the source plane.

 $P_0 = 3.2$ MPa, the peak axial positive pressures obtained using ANAH and k-wave are compared in Fig. 6(b) and (e). A good agreement is observed with a norm error of $L_2 = 6.2\%$ for the multilayer domain and an error of $L_2 = 4.1\%$ for the tumor case. Fig. 6(c) and (f) shows the detected harmonics at each propagation step. Due to the significant attenuation of soft tissue, the harmonic content is approximately an order of magnitude lower compared with the homogeneous water-like domain in Fig. 4(b). For the multilayer domain, a speed-up of 7.7 was achieved using the ANAH compared with the uniform mesh implementation with a calculated FRM value of 0.53. For the tumor domain, the speed-up was 9.5 with an FRM of 0.56. This investigation highlights the performance enhancement achieved using ANAH even when highly attenuating media are considered, and as a result, a relatively lower number of harmonics are generated. The implemented mixed-domain formulation is only accurate for weak heterogeneity and only considers the forward wave with no reflections [34]. For strongly heterogeneous media such as bone, reflection, phase, and amplitude corrections should be implemented to achieve accurate results [35]. Strongly heterogeneous media are going to be considered in the context of ANAH in future work.

D. Backward Propagation

In this section, we demonstrate ANAH for backward propagation. Here, the signal is downsampled as higher harmonics

TABLE I
TISSUE ACOUSTICAL PROPERTIES

	Nonlin. coeffi- cient	Speed of sound m/s	Density kg/m ³	Atten. coef.@ 1MHz (dB/cm)	Power law exponent
Water	5.8	1500	1000	0.05	2
Liver	4.3	1595	1060	0.5	2
Tumor	4.5	1563	1070	0.57	2

are decimated, and the field is propagated back to the source plane. This technique has potential applications in efficient nonlinear near-field acoustic holography [20], sound focusing and aberration correction [47], and cavitation mapping [48]. A desired field could also be generated synthetically and then projected backward to provide information on the source. Forward and backward iterations are used to obtain the geometry of acoustic holographic lenses or metasurfaces [10]. Implementing ANAH in this context can significantly reduce the computation time required to generate the necessary geometry for generating complex high-intensity nonlinear ultrasound fields.

Time reversal techniques are first used to obtain an image amplitude pressure distribution with an "ANAH" shape at a plane 25 mm away from the source plane, as shown in Fig. 7(a). The distributions of the peak positive pressure

and phase of the source are shown in Fig. 7(b) and (c), respectively. ANAH is then implemented to back propagate the field from the image plane back to the source plane. The pressure and phase values along the dashed line are compared in Fig. 7(d) and (e), respectively. The dashed line intersects the image plane's maximum peak positive pressure. The back propagation using ANAH produces good agreement with the initial source pressure, with a calculated norm error of $L_2 = 6.45\%$. The phases at the source plane are also in good agreement. To investigate the harmonic levels of the back propagated signal at the source plane, the total harmonic distortion [5] at each point was calculated. The signal exhibits low harmonic level with an average total harmonic distortion of 0.93%, showing accurate decimation of the harmonics in the back propagation. This indicates that ANAH is an effective tool for efficiently projecting a desired nonlinear field backward to provide information on the source. Finally, Fig. 7(f) illustrates the downsampling process where the Nyquist frequency gradually decreases as harmonics are decimated and the signal is propagated back to the source plane.

IV. CONCLUSION

An adaptive numerical algorithm for computationally efficient nonlinear acoustic holography is presented in this article. At each propagation step, the algorithm implements a monitoring function that tracks the harmonic content of the acoustic signal. The algorithm then adjusts the discretization parameters, namely, the step size and the temporal sampling rate, according to the frequency of the highest detected harmonic. The signal is upsampled in the frequency domain to accommodate the generated harmonics by maintaining a spectral buffer and zero-padding the spectrum of the signal. This ensures that the discretization parameters are gradually refined and that the higher harmonics are only resolved locally in regions of high nonlinearity. Our results demonstrate that the proposed implementation can significantly reduce the computational cost for highly nonlinear 3-D problems, achieving a speedup of up to nearly 50 times compared with a uniform mesh. Furthermore, the proposed adaptive algorithm was also used for backward propagation, which involves projecting the signal back to the source while gradually downsampling the signal as higher harmonics are decimated. To perform downsampling, the spectrum of the acoustic signal was truncated based on its harmonic content at each propagation step. The developed algorithm has numerous practical applications in nonlinear medical and physical acoustics. It allows for accurate HIFU source characterization and identification, as well as the prediction of sonication dosage and ultrasound-induced thermal effects. It can also be used to efficiently generate acoustic holographic lenses or metasurfaces for use in nonlinear applications. The adaptive algorithm for strongly heterogeneous media will be implemented in the future to allow accurate modeling of therapeutic procedures through aberrating layers.

The algorithm can be readily integrated with the MATLAB open-source toolbox mSOUND. The current implementation

for 2-D and 3-D problems as well as the instructions for integrating it with mSOUND are freely available [49].

REFERENCES

- [1] P. B. Rosnitskiy et al., "Design of HIFU transducers for generating specified nonlinear ultrasound fields," *IEEE Trans. Ultrason., Ferroelectr., Freq. Control*, vol. 64, no. 2, pp. 374–390, Feb. 2017.
- [2] O. V. Bessonova, V. A. Khokhlova, M. R. Bailey, M. S. Canney, and L. A. Crum, "Focusing of high power ultrasound beams and limiting values of shock wave parameters," *Acoust. Phys.*, vol. 55, nos. 4–5, pp. 463–473, Oct. 2009.
- [3] Y.-N. Wang, T. Khokhlova, M. Bailey, J. H. Hwang, and V. Khokhlova, "Histological and biochemical analysis of mechanical and thermal bioeffects in boiling histotripsy lesions induced by high intensity focused ultrasound," *Ultrasound Med. Biol.*, vol. 39, no. 3, pp. 424–438, Mar. 2013.
- [4] M. S. Canney, M. R. Bailey, L. A. Crum, V. A. Khokhlova, and O. A. Sapozhnikov, "Acoustic characterization of high intensity focused ultrasound fields: A combined measurement and modeling approach," *J. Acoust. Soc. Amer.*, vol. 124, no. 4, pp. 2406–2420, Oct. 2008.
- [5] A. Bhargava, V. C. Meesala, M. R. Hajj, and S. Shahab, "Nonlinear effects in high-intensity focused ultrasound power transfer systems," *Appl. Phys. Lett.*, vol. 117, no. 6, Aug. 2020, Art. no. 064101.
- [6] A. Sallam, E. Hoffmann, and S. Shahab, "Noninvasive deep stimulation of the brain via low-intensity holographic-focused ultrasound," *Proc.* SPIE, vol. 12483, Apr. 2023, Art. no. PC1248305.
- [7] P. V. Yuldashev and V. A. Khokhlova, "Simulation of three-dimensional nonlinear fields of ultrasound therapeutic arrays," *Acoust. Phys.*, vol. 57, no. 3, pp. 334–343, May 2011.
- [8] A. Simon et al., "Histotripsy for the treatment of uterine leiomyomas: A feasibility study in ex vivo uterine fibroids," *Ultrasound Med. Biol.*, vol. 48, no. 8, pp. 1652–1662, Aug. 2022.
- [9] V. S. Bachu, J. Kedda, I. Suk, J. J. Green, and B. Tyler, "High-intensity focused ultrasound: A review of mechanisms and clinical applications," *Ann. Biomed. Eng.*, vol. 49, no. 9, pp. 1975–1991, Sep. 2021.
- [10] A. Sallam and S. Shahab, "On nonlinear effects in holographic-modulated ultrasound," Appl. Phys. Lett., vol. 121, no. 20, Nov. 2022, Art. no. 204101.
- [11] A. Sallam, V. C. Meesala, M. R. Hajj, and S. Shahab, "Holographic mirrors for spatial ultrasound modulation in contactless acoustic energy transfer systems," *Appl. Phys. Lett.*, vol. 119, no. 14, Oct. 2021, Art. no. 144101.
- [12] A. Sallam and S. Shahab, "Acoustic lenses for generating high-intensity ultrasonic fields," *Proc. SPIE*, vol. 12043 Apr. 2022, Art. no. PC12043.
- [13] K. Melde, A. G. Mark, T. Qiu, and P. Fischer, "Holograms for acoustics," *Nature*, vol. 537, no. 7621, pp. 518–522, Sep. 2016.
- [14] A. Sallam, V. C. Meesala, and S. Shahab, "Theoretical and experimental investigations on metallic acoustic lenses," *Proc. SPIE*, vol. 11588, Mar. 2021, Art. no. 1158807.
- [15] A. Sallam and S. Shahab, "Tailoring nonlinear ultrasound beams using acoustic lenses," *J. Acoust. Soc. Amer.*, vol. 153, no. supplement 3, p. A236, Mar. 2023.
- [16] M. Bakhtiari-Nejad, A. Elnahhas, M. R. Hajj, and S. Shahab, "Acoustic holograms in contactless ultrasonic power transfer systems: Modeling and experiment," *J. Appl. Phys.*, vol. 124, no. 24, Dec. 2018, Art. no. 244901.
- [17] M. A. S. Ahmed and S. Shahab, "On guiding elastic waves in multi-layered solid media," *Proc. SPIE*, vol. 12483, Apr. 2023, Art. no. PC124830L.
- [18] A. Randad, M. A. Ghanem, M. R. Bailey, and A. D. Maxwell, "Design, fabrication, and characterization of broad beam transducers for fragmenting large renal calculi with burst wave lithotripsy," *J. Acoust. Soc. Amer.*, vol. 148, no. 1, pp. 44–50, Jul. 2020.
- [19] M. A. B. Andrade, T. S. Ramos, F. T. A. Okina, and J. C. Adamowski, "Nonlinear characterization of a single-axis acoustic levitator," *Rev. Sci. Instrum.*, vol. 85, no. 4, Apr. 2014, Art. no. 045125.
- [20] Y. Niu and Y.-J. Kim, "Nonlinear, dissipative, planar nearfield acoustical holography based on Westervelt wave equation," *J. Sound Vibrat.*, vol. 332, no. 4, pp. 952–967, Feb. 2013.
- [21] F. Varray, A. Ramalli, C. Cachard, P. Tortoli, and O. Basset, "Fundamental and second-harmonic ultrasound field computation of inhomogeneous nonlinear medium with a generalized angular spectrum method," *IEEE Trans. Ultrason., Ferroelectr., Freq. Control*, vol. 58, no. 7, pp. 1366–1376, Jul. 2011.

- [22] J. Jaros, A. P. Rendell, and B. E. Treeby, "Full-wave nonlinear ultrasound simulation on distributed clusters with applications in high-intensity focused ultrasound," *Int. J. High Perform. Comput. Appl.*, vol. 30, no. 2, pp. 137–155, May 2016.
- [23] J. Tavakkoli, D. Cathignol, R. Souchon, and O. A. Sapozhnikov, "Modeling of pulsed finite-amplitude focused sound beams in time domain," *J. Acoust. Soc. Amer.*, vol. 104, no. 4, pp. 2061–2072, Oct. 1998.
- [24] J. Tavakkoli and S. Mashouf, "Nonlinear acoustic beam propagation modeling in dissipative media," *Can. Acoust.*, vol. 39, no. 4, pp. 19–25, 2011.
- [25] V. A. Khokhlova, R. Souchon, J. Tavakkoli, O. A. Sapozhnikov, and D. Cathignol, "Numerical modeling of finite-amplitude sound beams: Shock formation in the near field of a cw plane piston source," *J. Acoust. Soc. Amer.*, vol. 110, no. 1, pp. 95–108, Jul. 2001.
- [26] R. J. Zemp, J. Tavakkoli, and R. S. C. Cobbold, "Modeling of nonlinear ultrasound propagation in tissue from array transducers," *J. Acoust. Soc. Amer.*, vol. 113, no. 1, pp. 139–152, Jan. 2003.
- [27] F. A. Duck, A. C. Baker, and H. C. Starritt, Ultrasound in Medicine. Boca Raton, FL, USA: CRC Press, 2020.
- [28] S. P. Groth et al., "Accelerating frequency-domain numerical methods for weakly nonlinear focused ultrasound using nested meshes," *J. Acoust. Soc. Amer.*, vol. 150, no. 1, pp. 441–453, Jul. 2021.
- [29] B. E. Treeby, "Modeling nonlinear wave propagation on nonuniform grids using a mapped k-space pseudospectral method," *IEEE Trans. Ultrason., Ferroelectr., Freq. Control*, vol. 60, no. 10, pp. 2208–2213, Oct. 2013.
- [30] Y. Jing, M. Tao, and J. Cannata, "An improved wave-vector frequency-domain method for nonlinear wave modeling," *IEEE Trans. Ultrason.*, Ferroelectr., Freq. Control, vol. 61, no. 3, pp. 515–524, Mar. 2014.
- [31] J. Gu and Y. Jing, "MSOUND: An open source toolbox for modeling acoustic wave propagation in heterogeneous media," *IEEE Trans. Ultrason.*, *Ferroelectr.*, *Freq. Control*, vol. 68, no. 5, pp. 1476–1486, May 2021.
- [32] Y. Jing, M. Tao, and G. T. Clement, "Evaluation of a wave-vector-frequency-domain method for nonlinear wave propagation," *J. Acoust. Soc. Amer.*, vol. 129, no. 1, pp. 32–46, Jan. 2011.
- [33] Y. Jing, "On the use of an absorption layer for the angular spectrum approach (L)," J. Acoust. Soc. Amer., vol. 131, no. 2, pp. 999–1002, Feb. 2012.
- [34] J. Gu and Y. Jing, "Numerical modeling of ultrasound propagation in weakly heterogeneous media using a mixed-domain method," *IEEE Trans. Ultrason., Ferroelectr., Freq. Control*, vol. 65, no. 7, pp. 1258–1267, Jul. 2018.
- [35] J. Gu and Y. Jing, "A modified mixed domain method for modeling acoustic wave propagation in strongly heterogeneous media," *J. Acoust.* Soc. Amer., vol. 147, no. 6, pp. 4055–4068, Jun. 2020.
- [36] Y. Jing and G. T. Clement, "On the use of Gegenbauer reconstructions for shock wave propagation modeling," in *Proc. IEEE Int. Ultrason. Symp.*, Oct. 2010, pp. 2052–2055.
- [37] V. Välimäki and S. Bilbao, "Giant FFTs for sample-rate conversion," J. Audio Eng. Soc., vol. 71, no. 3, pp. 88–99, Mar. 2023.
- [38] J. Adams, "A subsequence approach to interpolation using the FFT," IEEE Trans. Circuits Syst., vol. CS-34, no. 5, pp. 568–570, May 1987.
- [39] B. E. Treeby, J. Jaros, A. P. Rendell, and B. T. Cox, "Modeling nonlinear ultrasound propagation in heterogeneous media with power law absorption using a k-space pseudospectral method," *J. Acoust. Soc. Amer.*, vol. 131, no. 6, pp. 4324–4336, Jun. 2012.
- [40] E. Martin, J. Jaros, and B. E. Treeby, "Experimental validation of k-Wave: Nonlinear wave propagation in layered, absorbing fluid media," *IEEE Trans. Ultrason., Ferroelectr., Freq. Control*, vol. 67, no. 1, pp. 81–91, Jan. 2020.

- [41] K. Wang, E. Teoh, J. Jaros, and B. E. Treeby, "Modelling nonlinear ultrasound propagation in absorbing media using the k-Wave toolbox: Experimental validation," in *Proc. IEEE Int. Ultrason. Symp.*, Oct. 2012, pp. 523–526.
- [42] B. E. Treeby and B. T. Cox, "k-Wave: MATLAB toolbox for the simulation and reconstruction of photoacoustic wave fields," *J. Biomed. Opt.*, vol. 15, no. 2, 2010, Art. no. 021314.
- [43] k-Wave. Free Source K-Wave. Accessed: May 1, 2023. [Online]. Available: http://www.k-wave.org
- [44] B. E. Treeby, E. S. Wise, F. Kuklis, J. Jaros, and B. T. Cox, "Nonlinear ultrasound simulation in an axisymmetric coordinate system using a k-space pseudospectral method," *J. Acoust. Soc. Amer.*, vol. 148, no. 4, pp. 2288–2300, Oct. 2020.
- [45] L. E. Kinsler, A. R. Frey, A. B. Coppens, and J. V. Sanders, Fundamentals of Acoustics. Hoboken, NJ, USA: Wiley, 2000.
- [46] Y. Saijo and H. Sasaki, "High frequency acoustic properties of tumor tissue," in *Ultrasonic Tissue Characterization*. Cham, Switzerland: Springer, 1996, pp. 217–229.
- [47] G. T. Clement and K. Hynynen, "A non-invasive method for focusing ultrasound through the human skull," *Phys. Med. Biol.*, vol. 47, no. 8, pp. 1219–1236, Apr. 2002.
- [48] C. D. Arvanitis, C. Crake, N. McDannold, and G. T. Clement, "Passive acoustic mapping with the angular spectrum method," *IEEE Trans. Med. Imag.*, vol. 36, no. 4, pp. 983–993, Apr. 2017.
- [49] A. Sallam and S. Shahab. (2023). Adaptive Nonlinear Acoustic Holography. [Online]. Available: https://github.com/ahmedsallamholo/ANAH



Ahmed Sallam received the B.Sc. degree in mechanical engineering from the Jordan University of Science and Technology, Irbid, Jordan, in 2019. He is currently pursuing the Ph.D. degree with the Department of Mechanical Engineering, Virginia Tech, Blacksburg, VA, USA.

His research interests include linear and nonlinear ultrasound, ultrasound manipulation, acoustic holography, and acoustic lenses.



Shima Shahab received the M.S. and Ph.D. degrees in mechanical engineering with the Georgia Institute of Technology, Atlanta, GA, USA, in 2013 and 2015, respectively.

She is currently an Associate Professor of mechanical engineering with Virginia Tech, Blacksburg, VA, USA, and the Director of the Multiphysics Intelligent and Dynamical Systems (MInDS) Laboratory. The theoretical and experimental research programs at MInDS focus on structural dynamics and wave propagation

in ultrasound-responsive intelligent material systems. The various interdisciplinary applications include wireless ultrasound power transfer, acoustic holographic lenses, ultrasound atomization, and ultrasound-responsive polymer-based systems.